PAPER • OPEN ACCESS

Nonlinear dependence of plasma potential and ion impinging energy on energy loss of edge localized modes

To cite this article: S.Y. Dai and D.Z. Wang 2020 *Nucl. Fusion* **60** 026006

OPEN ACCESS
IOP Publishing | International Atomic Energy Agency
Nuclear Fusion
Nucl. Fusion **60** (2020) 026006 (6pp)
https://doi.org/10.1088/1741-4326/ab5a32

Nonlinear dependence of plasma potential and ion impinging energy on energy loss of edge localized modes

S.Y. Dai and D.Z. Wang

Key Laboratory of Materials Modification by Laser, Ion and Electron Beams (Ministry of Education), School of Physics, Dalian University of Technology, Dalian 116024, People's Republic of China

E-mail: daishuyu@dlut.edu.cn

Received 25 June 2019, revised 7 November 2019
Accepted for publication 21 November 2019
Published 20 December 2019

Abstract

Particle-in-cell (PIC) modelling has been performed to investigate the impact of energy loss during edge localized modes (ELMs) on the plasma potential and ion impinging energy on the divertor target. A double-peak structure of the ion impinging energy has been identified under JET-relevant ELM conditions. The ELM burst leads to a strong increase in the potential drop in front of the target plate, which accelerates the cold ions from the downstream divertor and accordingly causes a peak value of ion impinging energy. Moreover, the great potential drop helps confine the fast electrons and leads to a reduction in the potential drop and ion impinging energy. The arrival of the upstream hot ions results in the second peak value of ion impinging energy. The maximum potential drop and ion impact energy show a linear dependence on the pedestal temperature. Further, a nonlinear dependence of the peak potential drop and ion impact energy on the ELM energy loss can be ascertained based on the PIC simulations.

Keywords: particle-in-cell, edge localized modes, plasma sheath

(Some figures may appear in colour only in the online journal)

1. Introduction

Operation in high-confinement mode (H-mode) for tokamak devices is preferable due to improving particle confinement time and increasing density and temperature [1]. However, quasi-periodic occurrence of edge localized modes (ELMs) [2] in H-mode plasmas leads to a strong power leakage (ΔW_{ELMs}) of the plasma stored energy into the scrape-off layer (SOL) [3]. A major fraction of expelled high-energy particles end up at the downstream divertor [4, 5], which results in hazardous impacts such as severe wall erosion and short divertor lifetime [6–9]. Therefore, studies of ELM-induced sputtering of divertor targets are important for understanding the underlying mechanisms to explore the compatibility between H-mode plasmas and divertor performance.

Ion impinging energy on divertor targets is recognized as a primary parameter for calculating the physical sputtering of wall material [10]. Tungsten will be employed as the divertor target material in ITER due to its small physical sputtering yield and low co-deposited tritium inventory [11, 12]. The strong increase in the ion impinging energy during ELMs results in an increased sputtering of the tungsten material [13, 14]. A large impurity source of high-Z tungsten is intolerable due to severe bremsstrahlung in the core plasma, which can significantly deteriorate the energy confinement and even render the discharge termination [15]. The investigations of ELMs transport in SOL and power load on divertor targets have been carried out by the Vlasov [16–18], particle-in-cell (PIC) [13, 14, 19–23] and fluid [24] models. The code-code benchmark between different computational approaches shows reasonable agreement in the heat fluxes deposition on the divertor targets [25].

In our previous works, the PIC code has been extended to include the plasma wall interaction (PWI) module [26], which

Table 1. Summary of parameters used in SDPIC modelling.

Simulation parameters for JET ($\Delta W_{\mathrm{ELMs}} = 119$ KJ as the default case)			
Magnetic field strength (T)	2.4	Shortening factor	70
Pitch angle (°) 6	6	ELM crash duration t_{ELM} (μs)	200
Connection length L_{c} (m)	40	Pedestal plasma density Before ELM (m^{-3})	1.0×10^{19}
One half target-to-target poloidal length L_{pol} (m)	4.181	Pedestal temperature Before ELM (keV)	$T_{\mathrm{ped,e}} = 0.1$, $T_{\mathrm{ped,i}} = 0.2$
Parallel length of upstream source L_{s} (m)	25	Pedestal temperature during ELM (keV)	$T_{\mathrm{ped,e}} = T_{\mathrm{ped,i}} = 0.5$
Major radius R (m)	3	Particle source during ELM S_{p} (10^{26} m^{-3} s^{-1})	0.7
Simulation parameters for EAST ($\Delta W_{\mathrm{ELMs}} = 10.6$ KJ as the default case)			
Magnetic field strength (T)	2.25	Shortening factor	90
Pitch angle (°)	5	ELM crash duration t_{ELM} (μs)	200
Connection length L_{c} (m)	20	Pedestal plasma density before ELM (m^{-3})	1.0×10^{19}
One half target-to-target poloidal length L_{pol} (m)	1.743	Pedestal temperature before ELM (keV)	$T_{\mathrm{ped,e}} = 0.1$, $T_{\mathrm{ped,i}} = 0.2$
Parallel length of upstream source L_{s} (m)	12.5	Pedestal temperature during ELM (keV)	$T_{\mathrm{ped,e}} = T_{\mathrm{ped,i}} = 0.5$
Major radius R (m)	1.85	Particle source during ELM S_{p} (10^{26} m^{-3} s^{-1})	0.157

can provide the incident particles information and sputtering related data for other codes to mimic erosion process [27] and subsequent impurity transport [13]. Further, we study the influence of the plasma sheath evolution on the ion impact energy and the contribution of the potential drop to the ion impact energy during ELMs for EAST tokamak [14]. However, an important unresolved issue concerns that the role of the upstream ELM energy loss ΔW_{ELMs} affects the downstream sheath potential and ion impinging energy. The amplitude of ΔW_{ELMs} is strongly associated with the pedestal plasma temperature (T_{ped}) and the particle source (S_{p}). The measurements of the ion target impact energy on the JET experiments have been conducted by Langmuir probe and coupled infrared thermography, which indicates that the peak ion impact energy during ELMs has a linear dependence on T_{ped} [28]. Further, ELM-induced sudden increase in S_{p} can change the space charge distribution, which leads to a remarkable response of the plasma potential and ion impinging energy [14]. Hence, understanding the dependence of the potential drop and ion impact energy on ΔW_{ELMs} has a more general implication for estimating the ion impinging energy and the material sputtering yield.

In this work, the correlation of the plasma potential and ion impact energy with ΔW_{ELMs} is investigated by one-dimension-in-space and three-dimension-in-velocity (1d3v) PIC code SDPIC [13, 14]. The numerical algorithms of the SDPIC code and the comparison with the Type I ELMy H-mode experiments on EAST are introduced in [13]. In this study, the evolutions of potential drop and ion impinging energy are studied under the JET-relevant H-mode plasma conditions. The detailed analysis of dependence of maximum potential drop and ion impinging energy on T_{ped} and ΔW_{ELMs} has been conducted based on the SDPIC modelling results. Moreover, the same survey has been attempted for EAST case in order to make a comparative study for different size tokamaks. It is found that the amplitudes of the potential drop and ion impact energy are associated with the device size.

2. Methods and simulation setup

The ELMs modelling in SDPIC code is treated as before-ELM SOL source, ELM source and after-ELM SOL source (same as before-ELM). For the pre-ELM phase, the ions and electrons with a Maxwellian velocity distribution are injected into the simulation volume and tracked until a steady-state solution is obtained. The ELM burst is modelled as a transient source of plasma releasing the ELM energy loss ($\Delta W_{\mathrm{ELMs}} \sim T_{\mathrm{ped}} S_{\mathrm{p}} V_{\mathrm{src}} t_{\mathrm{ELM}}$) into the source volume V_{src} in the SOL for a period of the ELM crash duration t_{ELM}. The spatial grid-cell size and the time step should be of the order of Debye length and the plasma oscillation period in the PIC simulation, respectively [29]. This indicates that an unrealistically large number of spatial grid cells is required for a real size tokamak SOL. In order to resolve this issue, the shortening technique commonly implemented into the PIC modes [13, 14, 19–21] for SOL modelling is employed to reduce the computational size and simulation time, which is achieved by increasing the collision frequency by a shortening factor k in the upstream plasma while the sheath remains unchanged. Increase in the collisionality results in a reduction in the mean free path length as well as time and size of the PIC model according to [19–21]. In order to discuss the simulation results in a real SOL size, it is necessary to rescale the simulation data by the shortening factor k for the shortened size and time. Here, it is noted that the domain length and transit times discussed in later text and figures have been converted to the situation with a real SOL size.

In this work, the geometric and plasma parameters are specified according to the typical H-mode discharge with ELMs on JET [5, 21, 25]. Table 1 presents the summary of parameters used in SDPIC modelling. The major radius of JET $R = 3.0$ m, the connection length $L_{\mathrm{c}} = 40$ m and the shortening factor $k = 70$ are used for JET modelling. The magnetic field strength $B = 2.4$ T and pitch angle $\alpha = 6°$ are employed. One half of the target-to-target poloidal length ($L_{\mathrm{pol}} = L_{\mathrm{c}} \sin\alpha$) is about 4.181 m. The parallel length of the upstream source $L_{\mathrm{s}} = 25$ m is used where hot particles are released. The pedestal plasma density $n_{\mathrm{ped}} = 1.0 \times 10^{19}$ m^{-3}, electron temperature $T_{\mathrm{e}} = 100\,\mathrm{eV}$ and ion temperature $T\mathrm{i} = 200\,\mathrm{eV}$ are applied for the upstream source before ELM burst. The ELM is triggered at 28 μs in the SDPIC simulation when ELM-free plasma is in the steady-state. The transient burst of ELM releases an ELM energy loss

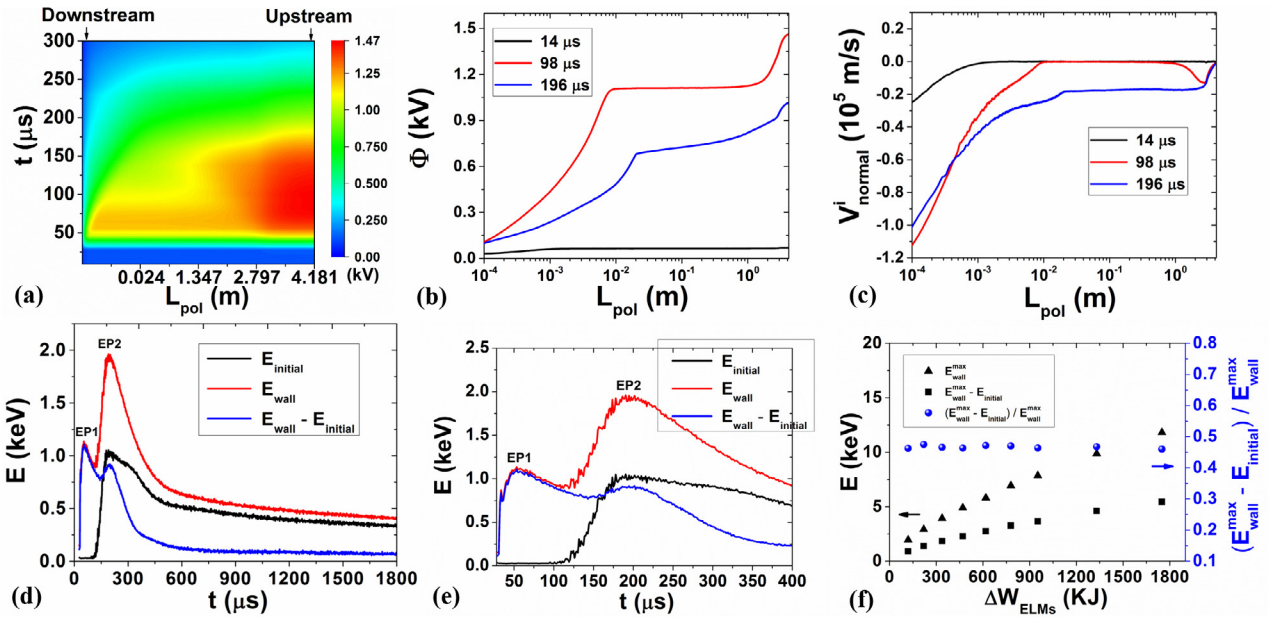

Figure 1. (*a*) Spatial and temporal evolutions of the plasma potential during ELM, (*b*) spatial evolution of the plasma potential for the pre-ELM (14 μs) and during ELM (98 and 196 μs) phases, (*c*) spatial evolution of the ion velocity along the normal to the wall for the pre-ELM (14 μs) and during-ELM (98 and 196 μs) phases, (*d*) time evolution of the ion initial energy ($E_{\rm initial}$), the ion impact energy ($E_{\rm wall}$) and their difference ($E_{\rm wall} - E_{\rm initial}$), (*e*) zoom-in profile of figure (*d*) and (*f*) profile of the peak ion impact energy, the corresponding energy difference induced by the potential drop and the ratio of the corresponding energy difference to the maximum ion impact energy against the ELM energy loss $\Delta W_{\rm ELMs}$. The start and end times of ELM burst are $t_{\rm start} = 28$ μs and $t_{\rm end} = 228$ μs, respectively.

$\Delta W_{\rm ELMs} = 119$ KJ into the upstream source region with an ELM crash duration $t_{\rm ELM} = 200$ μs, which is referred to as the default case in this study. The pedestal plasma temperature $T_{\rm ped,e} = T_{\rm ped,i} = 0.5$ keV and particle source $S_{\rm p} = 0.7 \times 10^{26}$ m^{-3} s^{-1} are employed for the upstream source during ELM. In addition, the simulation parameters for EAST reference case is also shown in table 1.

3. Results and discussion

Figure 1(*a*) displays the spatial and temporal evolutions of the plasma potential during ELM for JET case. The spatial dimension of the simulation domain for ELM modelling is described as the poloidal length ($L_{\rm pol}$) in figure 1(*a*), which is non-uniform due to the use of the shortening technique as mentioned above. The positions of the downstream divertor and upstream SOL are indicated to clearly mark the spatial evolution of the potential drop. The transit time scale for the upstream ELM electrons is evaluated as $\tau_{\rm e} \approx L_{\rm c}/v_{\rm th}^{\rm e} \approx 4$ μs, where $v_{\rm th}^{\rm e}$ is the electron thermal velocity at the pedestal. The propagation time scale $\tau_{\rm i}$ for the upstream ELM ions is about 183 μs ($\tau_{\rm i} \approx L_{\rm c}/c_{\rm s}$, $c_{\rm s}$ is the ion sound speed at the pedestal). Hence, the fast transit of electrons can lead to a strong space charge separation after triggering the ELM and accordingly a great evolution of plasma potential as shown in figure 1(*a*). The peak value of the space potential is about 1.47 keV for the default case. The spatial evolutions of the plasma potential and ion velocity along the normal to the wall for the pre-ELM (14 μs) and during-ELM (98 and 196 μs) phases are presented in figures 1(*b*) and (*c*), respectively. For the case of 98 μs, it can be calculated that the upstream ELM ions arrive at the location of $L_{\rm pol} \approx 2.6$ m. The increased ion velocity around $L_{\rm pol} = 2.6$ m can also be seen for 98 μs in figure 3(*c*). While for 196 μs, the main ELM ions are delivered to the position of $L_{\rm pol} \approx 0.3$ m. Hence, the ion velocity between $L_{\rm pol} = 0.3$ and 2.6 m for 196 μs is higher than that for the cases of 14 and 98 μs in figure 1(*c*). The significant potential drops during ELMs near the wall ($L_{\rm pol} \sim 10^{-2}$ m) in figure 1(*b*) lead to an intense acceleration of the ion velocity in figure 1(*c*). The higher potential drop (~1.1 kV) for 98 μs results in a larger ion velocity on the wall compared to the cases of 14 and 196 μs. Based on the above simulation results, the detailed analysis of the influence of ELM-induced potential evolution on the ion impact energy has been performed in the current work, which is presented in figures 1(*d*)–(*f*) below. In addition, the potential evolution and the associated ion acceleration during ELMs were also studied by the BIT1 modelling in [5, 20, 21].

The impact of the strong evolution of the plasma potential on the ion impinging energy is studied by comparing the ion initial energy ($E_{\rm initial}$) and ion impinging energy ($E_{\rm wall}$). Since $E_{\rm initial}$ is recorded for each simulated particle in SDPIC, the distribution of $E_{\rm wall}$ can be obtained after the bombardment of the incident ions on the wall. In principle, the influence of the potential drop on the ion impact energy during ELM can be analysed by the energy difference ($E_{\rm wall} - E_{\rm initial}$). An interesting double-peak structure (labelled as the EP1 and EP2) of the ion impinging energy can be seen in figure 1(*d*). At the beginning phase of ELM, the great potential drop induced by the fast electrons leads to a steep increase in the ion impinging energy, which are mainly from the cold ions with a very low initial energy near the target plate. However, the energy difference and the ion impinging energy decrease after around

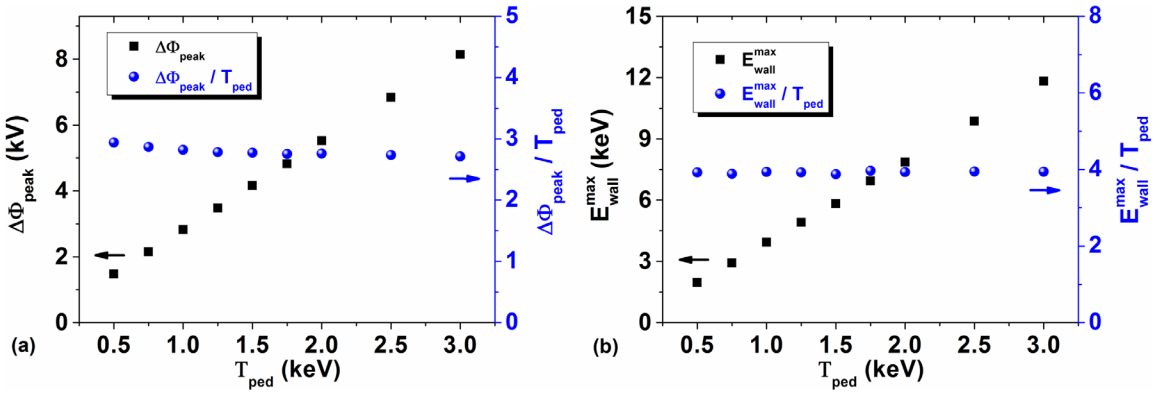

Figure 2. Profiles of the maximum potential drop ($\Delta\varphi_{\rm peak}$) and the ratio $\Delta\varphi_{\rm peak}/T_{\rm ped}$ (a) and the peak value of ion impact energy ($E_{\rm wall}^{\rm max}$) and the ratio $E_{\rm wall}^{\rm max}/T_{\rm ped}$ (b) against the pedestal temperature $T_{\rm ped}$ for JET case.

Table 2. Simulation parameters of pedestal temperature and particle source for different ELM energy losses during ELMs for JET and EAST cases.

Simulation parameters for JET									
$T_{\rm ped,e,i}$ (keV)	0.5	0.75	1.0	1.25	1.5	1.75	2.0	2.5	3.0
$S_{\rm p}$ (10^{26} m^{-3} s^{-1})	0.7	0.86	0.995	1.11	1.22	1.32	1.41	1.57	1.72
$\Delta W_{\rm ELMs}$ (KJ)	119	219	337	470	618	779	952	1330	1749
Simulation parameters for EAST									
$T_{\rm ped,e,i}$ (keV)	0.5	0.75	1.0	1.25	1.5				
$S_{\rm p}$ (10^{26} m^{-3} s^{-1})	0.157	0.192	0.222	0.248	0.272				
$\Delta W_{\rm ELMs}$ (KJ)	10.6	19.5	30	42	55				

50 μs as shown in figure 1(e). The potential drop in figure 1(a) causing the energy difference in figure 1(e) reduces gradually in front of the divertor target. The great potential hill (>1 kV) near the target prevents the fast electrons ($T_{\rm ped} = 0.5$ keV) from surmounting the repulsive sheath and reaching the wall surface. The deceleration of the upstream electrons leads to a suppression of the space charge separation and a resulting pullback of the potential drop, which results in a decrease of the ion impinging energy in figure 1(e). This pullback of the potential drop was not discovered in the previous study of EAST case [14] because the potential hill near the target is too low to obstruct upstream fast electrons. The upstream high energy ions lead to an increase of the ion impact energy after about 125 μs. The second peak value of the ion impact energy is obtained around 200 μs along with the arrival of the upstream bulk plasma to the downstream divertor. The peak ion impact energy (~2 keV) is about four times larger than $T_{\rm ped} = 0.5$ keV, which has a good agreement with the experimental result on JET [28]. In addition, the second peak value of the energy difference is also obtained because the upstream ions can be adequately accelerated by the space potential. Finally, the ion impact energy decreases gradually after the termination of ELM burst.

The effect of the ELM energy loss on the ion impinging energy and potential drop for JET is studied in figure 1(f). Both the maximum ion impact energy and the corresponding energy difference increase with the ELM energy loss. In comparison with the EAST case for the same $T_{\rm ped}$ [14], the ELM power is much higher for JET due to the larger $S_{\rm p}$ and $V_{\rm src}$. The larger $S_{\rm p}$ can lead to a higher fast electron flux and an increased space charge separation on JET, which results in a higher potential drop and ion impact energy compared to EAST. Furthermore, the extent to which the ELM energy loss and the plasma potential affect the ion impinging energy for JET is investigated. The ratios of the corresponding energy difference to the maximum ion impact energy maintain about 0.46 for different ELM powers. The similar phenomena are also observed for the modelling of EAST, which shows that the contribution of the potential drop to the maximum ion impact energy is around 0.3 [14]. For the same $T_{\rm ped} = 0.5$ keV, the time interval between the maximum potential drop (EP1) and ion impact energy (EP2) is about 140 μs for JET ($\Delta W_{\rm ELMs} = 119$ KJ), while the time interval is around 80 μs for EAST ($\Delta W_{\rm ELMs} = 10.6$ KJ) [14]. The larger $L_{\rm c}$ for JET results in a longer transit time for the upstream ions which are unable to replenish the downstream plasma in time as well as EAST for the same $T_{\rm ped}$, which leads to a slower recovery of the potential drop for JET. Hence, the contribution of the potential drop to the maximum ion impact energy is stronger for JET.

Further, the impacts of pedestal temperature ($T_{\rm ped}$) on the peak potential drop and ion impact energy have been ascertained in figure 2. The upstream particle source $S_{\rm p}$ is governed by the parallel flux loss ($n_{\rm ped} * T_{\rm ped}^{0.5}$) along the open field line according to the [25, 30]. Hence, the change in $T_{\rm ped}$ would affect $S_{\rm p}$ as well. Moreover, it can be derived $\Delta W_{\rm ELMs} \sim (n_{\rm ped} V_{\rm src} t_{\rm ELM}) * T_{\rm ped}^{1.5}$ according to the above-mentioned relation ($\Delta W_{\rm ELMs} \sim T_{\rm ped} S_{\rm p} V_{\rm src} t_{\rm ELM}$). Table 2 shows the simulation

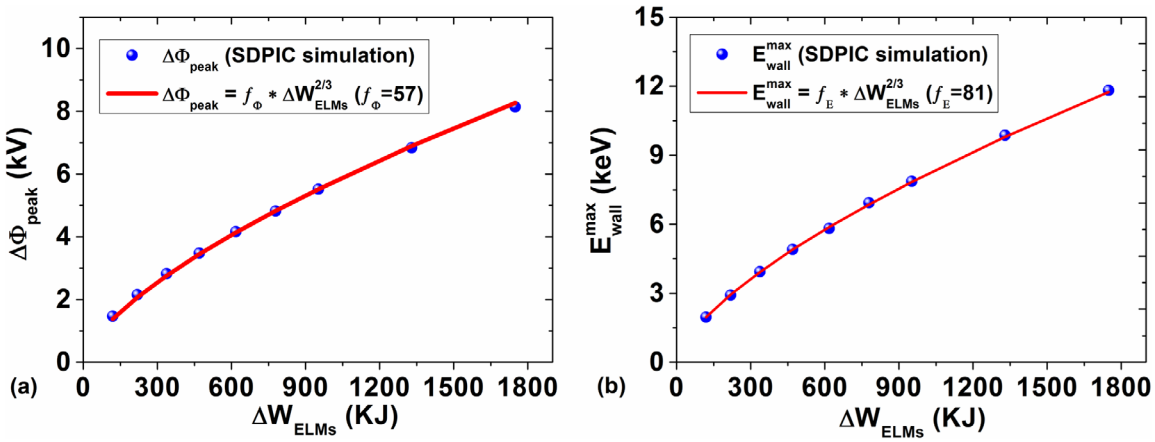

Figure 3. Profiles of the maximum potential drop by SDPIC simulation and the empirical formula $\Delta\varphi_{\rm peak} = f_\varphi * (\Delta W_{\rm ELMs})^{2/3}$, $f_\varphi = 57$ (*a*) and the peak value of ion impact energy by SDPIC simulation and the empirical formula $E_{\rm wall}^{\rm max} = f_{\rm E} * (\Delta W_{\rm ELMs})^{2/3}$, $f_{\rm E} = 81$ (*b*) for JET case.

parameters of pedestal temperature and particle source for different ELM energy losses during ELMs for JET and EAST cases. As the $T_{\rm ped}$ rises, the increased fast electron flux makes a stronger space charge separation and a larger peak value of the potential drop in figure 2(*a*). It is found that the ratio $\Delta\varphi_{\rm peak}/T_{\rm ped}$ maintains in the range from 2.7 to 3.0 for different $T_{\rm ped}$. Moreover, the peak value of the ion impact energy, which emerges behind the maximum potential drop, also increases with $T_{\rm ped}$. In particular, the simulated $E_{\rm wall}^{\rm max}$ has a four-fold linear relationship with $T_{\rm ped}$, which is in reasonable agreement with the JET experimental measurements [28]. In addition, the same calculations of $\Delta\varphi_{\rm peak}/T_{\rm ped}$ and $E_{\rm wall}^{\rm max}/T_{\rm ped}$ have been carried out for EAST, which also shows the linear relations $\Delta\varphi_{\rm peak}/T_{\rm ped} \approx 1$ and $E_{\rm wall}^{\rm max}/T_{\rm ped} \approx 2$, respectively. The different ratios in $\Delta\varphi_{\rm peak}/T_{\rm ped}$ and $E_{\rm wall}^{\rm max}/T_{\rm ped}$ between JET and EAST are mainly due to different geometrical sizes and ELM powers for both devices. The larger $L_{\rm c}$ and higher $S_{\rm p}$ for JET lead to a stronger potential drop and a bigger ion impinging energy compared to EAST as mentioned above.

A further analysis of the relation of the peak potential drop and ion impact energy with the ELM energy loss is performed in figure 3, which can include both information of $T_{\rm ped}$ and $S_{\rm p}$. Since $\Delta\varphi_{\rm peak}$ and $E_{\rm wall}^{\rm max}$ have a linear dependence on $T_{\rm ped}$, as shown in figure 2, $\Delta\varphi_{\rm peak}$ and $E_{\rm wall}^{\rm max}$ can be expressed as the empirical formulae of $\Delta\varphi_{\rm peak} = f_\varphi * (\Delta W_{\rm ELMs})^{2/3}$ and $E_{\rm wall}^{\rm max} = f_{\rm E} * (\Delta W_{\rm ELMs})^{2/3}$ in combination with the above-mentioned relation ($\Delta W_{\rm ELMs} \sim T_{\rm ped}^{1.5}$), respectively. Here, the coefficients f_φ and $f_{\rm E}$ can be estimated according to the results in figure 2. Figure 3 shows the maximum potential drop and ion impact energy against $\Delta W_{\rm ELMs}$ by SDPIC simulations. The use of $f_\varphi = 57$ and $f_{\rm E} = 81$ in the empirical formulae for $\Delta\varphi_{\rm peak}$ and $E_{\rm wall}^{\rm max}$ gives a good agreement with the simulated data set by SDPIC, as shown in figure 3. The same attempt has been conducted for the EAST tokamak, which also shows the nonlinear dependence of $\Delta\varphi_{\rm peak}$ and $E_{\rm wall}^{\rm max}$ on $\Delta W_{\rm ELMs}$ with $f_\varphi = 110$ and $f_{\rm E} = 218$, respectively. The different coefficients are mainly associated with the dimensional difference between JET and EAST. The larger size of JET possesses a stronger $S_{\rm p}$ and also a bigger $V_{\rm src}$ and $L_{\rm c}$, which leads to a different ELM transport behaviour as mentioned above and resulting different coefficients between JET and EAST. The ELM energy loss for JET is around ten times higher than that for EAST for the same $T_{\rm ped}$. The respective maximum potential drop and ion impact energy for JET are enhanced by a factor of about 2.6 and 1.8 compared to EAST according to the above empirical formulae.

4. Conclusions

This study, for the first time, identifies that the maximum potential drop and ion impact energy during ELMs have a nonlinear dependence on the ELM energy loss. The empirical formulae derived from the numerical modelling can be used to make an analytic scaling of the peak potential drop and ion impact energy, which has a strong implication for estimating the sputtering yield induced by ELMs for tokamak devices. For JET-relevant ELM conditions, a double-peak structure of the ion impinging energy has been observed. The first peak value of the ion impact energy is due to the strong ELM-induced potential drop causing a significant increase in the impinging energy of the cold ions from the downstream divertor; and then the great potential hill near the target can help confine the fast electrons, which leads to a potential pullback; finally the second peak value is obtained by the upstream hot ions which can be adequately accelerated by the space potential. The peak potential drop and ion impact energy show a linear dependence on the pedestal temperature for both JET and EAST. The simulated maximum ion impact energy has a four-fold linear relationship with the pedestal temperature on JET, which is in reasonable agreement with the experimental measurements.

Acknowledgments

This work supported by National MCF Energy R&D Program of China Nos: 2018YFE0311100, 2018YFE0303105,

2017YFE0300501, 2017YFE0301206 and 2017YFE0300402, National Natural Science Foundation of China under Grant Nos. 11405021 and 11675037, High-level talent innovation support program of Dalian No. 2017RQ052, and the Fundamental Research Funds for the Central Universities No. DUT18LK03. The first author S.Y. Dai would like to express his appreciation to his wife Y.C. Li for understanding during manuscript revision and giving the birth to their son.

ORCID iDs

S.Y. Dai https://orcid.org/0000-0001-6384-8437
D.Z. Wang https://orcid.org/0000-0003-0517-7318

References

[1] Loarte A. *et al* 2007 *Nucl. Fusion* **47** S203
[2] Zohm H. 1996 *Plasma Phys. Control. Fusion* **38** 105
[3] Loarte A. *et al* 2003 *Plasma Phys. Control. Fusion* **45** 1549
[4] Pitts R.A. *et al* 2006 *Nucl. Fusion* **46** 82
[5] Pitts R.A. *et al* 2007 *Nucl. Fusion* **46** 1437
[6] Eich T. *et al* 2003 *Phys. Rev. Lett.* **91** 195003
[7] Eich T. *et al* 2011 *Phys. Rev. Lett.* **107** 215001
[8] Federici G. *et al* 2003 *Plasma Phys. Control. Fusion* **45** 1523
[9] Kreter A. *et al* 2009 *Phys. Rev. Lett.* **102** 045007
[10] Eckstein W. 2008 *Vacuum* **82** 930
[11] Pitts R.A. *et al* 2013 *J. Nucl. Mater.* **438** S48–56
[12] Doerner R.P. *et al* 2009 *Nucl. Fusion* **49** 035002
[13] Dai S.Y. *et al* 2015 *Nucl. Fusion* **55** 043003
[14] Dai S.Y. *et al* 2018 *Nucl. Fusion* **58** 014006
[15] Federici G. *et al* 2001 *Nucl. Fusion* **41** 1967
[16] Manfredi G. *et al* 2011 *Plasma Phys. Control. Fusion* **53** 015012
[17] Moulton D. *et al* 2013 *Plasma Phys. Control. Fusion* **55** 085003
[18] Coulette D. *et al* 2016 *Plasma Phys. Control. Fusion* **58** 085004
[19] Bergmann A. 2002 *Nucl. Fusion* **42** 1162
[20] Tskhakaya D. 2017 *Plasma Phys. Control. Fusion* **59** 114001
[21] Tskhakaya D. *et al* 2004 *Proc. 'Theory of Fusion Plasmas' (Bologna, Italy)* p 97
[22] Hosokawa M. 2016 *Plasma Fusion Res.* **11** 1403104
[23] Hosokawa M. *et al* 2018 *Proc. 45th EPS Conf. on Plasma Physics (Prague, Czech Republic, 2–6 July 2018)* p O2.110 (http://ocs.ciemat.es/EPS2018PAP/pdf/O2.110.pdf)
[24] Havlíčková E. *et al* 2011 *Plasma Phys. Control. Fusion* **53** 065004
[25] Havlíčková E. *et al* 2012 *Plasma Phys. Control. Fusion* **54** 045002
[26] Dai S.Y. *et al* 2014 *Nucl. Fusion* **54** 123015
[27] Dai S.Y. *et al* 2015 *J. Nucl. Mater.* **463** 372
[28] Guillemaut C. *et al* 2015 *Plasma Phys. Control. Fusion* **57** 085006
[29] Birdsall C.K. *et al* 1985 *Plasma Physics via Computer Simulation* (New York : McGraw-Hill)
[30] Loarte A. *et al* 2002 *Plasma Phys. Control. Fusion* **44** 1815